JOURNAL OF AIRCRAFT
Vol. 37, No. 6, November–December 2000

Simulation of Wake Vortex Detection with Airborne Doppler Lidar

Denis Darracq,* Alexandre Corjon,† and Frédéric Ducros‡
Centre Européen de Recherche et de Formation Avancée en Calcul Scientifique, 31057 Toulouse CEDEX, France
and
Mike Keane,§ Daniel Buckton,§ and Mike Redfern§
National University of Ireland, Galway, Ireland

A simulation approach is used to demonstrate that an airborne, forward-looking lidar can detect trailing wake vortices generated by a leading aircraft. Computational fluid dynamics techniques are used to generated flowfields containing wake vortices. These flowfields are applied to a Doppler lidar simulation model. The simulated geometry has the forward-looking lidar mounted on a following aircraft, whereas the wake vortices are generated by a leading aircraft. In such a configuration, it is not possible to directly detect the strong rotational velocity components of a wake vortex with a Doppler system; detection relies on the presence of induced axial velocity signatures. We demonstrate that axial flows are induced as the vortices evolve, and that these axial flows can be detected with a Doppler lidar system.

Nomenclature

A, Q	= atmosphere boundary-layer (ABL) parameters, temperature gradient and ground heat flux
b_0	= initial spacing between vortices
C_K	= Kolmogorov constant
h	= altitude, height of ABL or vortices
P	= pressure
r_c	= core radius
t	= time relative to vortex creation by leading aircraft
$\boldsymbol{u}$	= velocity vector
V_0	= maximal tangential velocity
x, y, z	= ground coordinate
$\boldsymbol{x}$	= position vector
α, β	= Lamb–Oseen related constants
ν_t	= turbulent viscosity
ρ	= density

I. Introduction

WAKE vortices, the rotating columns of turbulent air shed from the wing tips of all aircraft and left behind in their wake, are a potential hazard to other aircraft encountering them. The main hazard associated with wake vortex encounter occurs when the following aircraft happens to fly along the axis of rotation of a trailing wake vortex. If this occurs, the vortex can effect a potentially hazardous rolling moment on the following aircraft, especially if it is in a low-airspeed, low-altitude state, as is usual for aircraft approaching touchdown.

Following a first study program, carried out by the Federal Aviation Administration between 1969 and 1970, the International Civil Aviation Organization (ICAO) defined takeoff and landing separation standards based on a 3 × 3 matrix of Maximum Take-Off Weights (MTOW). The objective of this categorization is to ensure safety by avoiding any encounter between trailing wake vortices and following aircraft. However, as a result of constant traffic growth, these separations now limit capacity at busy airports.

Current separation standards are conservative, as an actual wake vortex rarely remains stable long enough to pose a hazard to following aircraft. In addition, wake vortices that do remain stable are often moved out of the landing corridor by cross winds.

In the United States, landing separation distances are relaxed under Visual Flight Rules (VFR): the pilot is normally requested to visually maintain safe separation from the leading aircraft. Under Instrument Flight Rules (IFR), MTOW separations are applied. The difference between IFR separation and the reduced, yet apparently safe, VFR separation, have led researchers to conclude that the IFR regulations may be unnecessarily conservative.[1]

Considerable research effort is currently focused on technologies that will allow for a reduction in aircraft landing spacing under appropriate conditions.[2] It is expected that technology capable of detecting wake vortices in real time will play an important part in reducing aircraft landing separation. Ground based, Doppler lidar systems have already been proven capable of detecting trailing wake vortices from landing aircraft.[3]

Currently, a European consortium (described in the Acknowledgments) is investigating the feasibility of detecting wake vortices using an airborne, Doppler lidar system. It is envisaged that aircraft equipped with such a system could safely follow leading aircraft at a significantly reduced separation. This paper describes the simulation experiments that were carried out as part of the system feasibility study.

II. Airborne Lidar Systems

Lidar is an acronym derived from light detection and ranging and is a concept similar to radar. Atmospheric Doppler lidar systems use optical instrumentation to transmit a coherent, narrow band, laser pulse into the atmosphere along a narrow path known as a line of sight. The narrow beam and the absence of side lobes mean that lidar systems are not affected by the problem of ground clutter that is associated with radar systems.

As the optical pulse travels out along the line of sight, it encounters a distributed ensemble of aerosol particles. These particles scatter a portion of the incident pulse energy; some of which is scattered back to the receiver. At optical wavelengths, the bulk of the backscattered energy from the atmosphere is contributed by particles with diameters less than 3 μm; these particles are small enough to be advected

Presented as Paper 98-0666 at the AIAA 36th Aerospace Sciences Meeting, Reno, NV, 12–15 January 1998; received 17 August 1998; revision received 25 March 2000; accepted for publication 9 May 2000.

*Senior Research Scientist, Computational Fluid Dynamics Team, 42 av. Gaspard Coriolis; darracq@cerfacs.fr. Member AIAA.
†Senior Research Scientist, Computational Fluid Dynamics Team. Member AIAA.
‡Senior Research Scientist, Computational Fluid Dynamics Team.
§Research Scientist, Applied Imaging Research Group, Department of Experimental Physics.

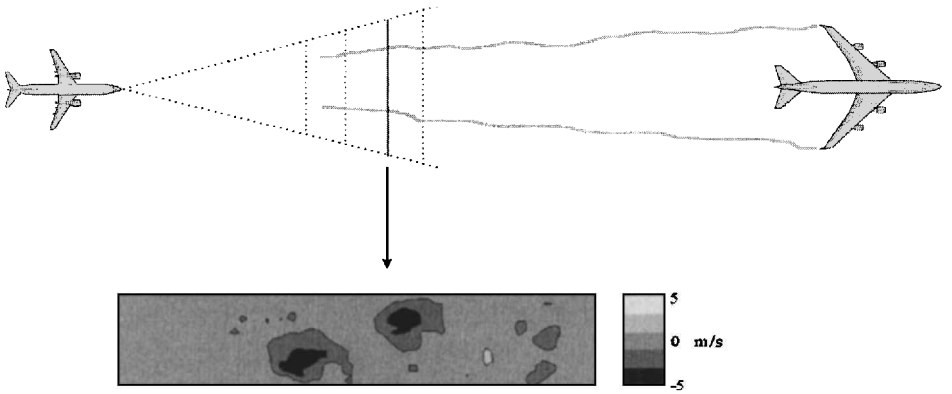

Fig. 1 Schematic of the forward looking Doppler lidar system mounted on a following aircraft showing how velocity images are formed. The typical radial velocity image shown here was formed 1000 m ahead of the following aircraft.

by the wind and thus serve as effective wind tracers.[4] Thus, the energy back scattered by an aerosol is Doppler shifted by a frequency $f = 2v/\lambda$, where v is the radial component of wind velocity, i.e., the velocity component parallel to the direction of propagation of the pulse, and λ is the laser wavelength.

Because the atmospheric aerosols form a distributed target, a continuous backscattered signal is present at the system receiver as the pulse propagates away from the lidar. This returned signal is optically heterodyned with a stable local oscillator in order to shift the Doppler shifted signal down to the radio frequency range. Analog processing of the electrical photodetector signal is then used to remove the Doppler shift due to the forward motion of the aircraft. The resulting signal is digitally sampled and time-gated, in order to produce range resolved measurements. The Doppler shift within each gate is estimated using digital frequency estimation methods.

Ground-based atmospheric mapping with Doppler lidar has been under development since 1966 and is now a mature technology.[4] Recently, a number of airborne Doppler lidar systems have been developed and successfully tested. These include the U.S. Air Force C-130 downward-looking lidar that is being developed for use in airborne ballistic operations[5] and the forward looking ACLAIM system,[6] developed by NASA, which has been used to demonstrate airborne look-ahead turbulence detection and warning.

In this paper, the potential ability of an airborne Doppler lidar to detect wake vortices generated by a leading aircraft is investigated by simulation. The proposed system uses a 2 μm pulsed lidar and a forward-looking, two-dimensional scanner to interrogate the airspace into which the following aircraft will fly. This concept is illustrated in Fig. 1. The lidar performance parameters used for this investigation are similar to those already achieved in existing airborne systems.

III. Approach

In a Doppler lidar, only the component of the air velocity in the direction of propagation of the lidar beam causes a Doppler shift in the returned signal. Hence, it is not possible to directly detect the rotational velocity component of a wake vortex while viewing it axially. Consequently, detection of wake vortices generated by leading aircraft with a forward-looking Doppler system relies on the presence of identifiable axial velocity signatures.

The generation of an axial velocity in the core as part of wake vortex roll-up was shown by Brown.[7] However, this initial axial velocity holds only at relatively short distances behind the wing, where the spiral system is well rolled up, but before the vortex has spread and been reduced in intensity by turbulent diffusion. Much farther back from the wing, the development of axial velocity characteristics in the vortex core, as a result of axial pressure gradients, was theoretically predicted by Batchelor.[8]

In this paper, we are interested in detecting wake vortices that pose a hazard to following aircraft by detecting the axial velocity components predicted by Batchelor. To investigate the feasibility of such detection, large eddy simulations (LESs), using two different turbulence models, are used to simulate the evolution of wake vortices

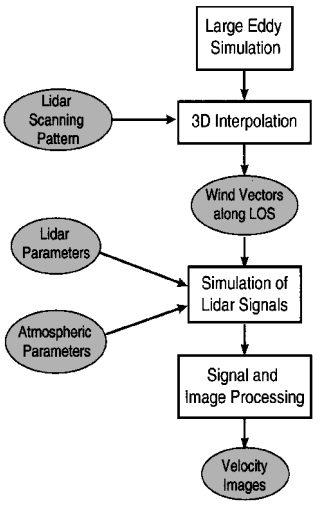

Fig. 2 Overview of simulation of forward-looking Doppler lidar system.

in different turbulence conditions. In each case, the vortices are initialized in a rolled-up state without any axial velocity components. As the vortices evolve in the LES, the vortices stretch and deform, and axial components are induced in and near the vortex cores.

The three-dimensional flowfields from the LES are applied to a software simulation of the proposed airborne Doppler lidar system. Other inputs to the Doppler lidar simulation system are the lidar performance parameters, the atmospheric parameters, the scanning pattern, and the measurement geometry. An overview of the method that we use to simulate the performance of an airborne Doppler lidar system is shown in Fig. 2.

The simulation system also incorporates the signal processing and image processing algorithms that have been developed for use in an actual system. The output of the simulation system is a set of image processed radial velocity images. Our results indicate that axial velocity components induced in the cores of wake vortices can be detected in these images.

The following section describes the LES of wake vortices. Section V gives details of the method used to simulate the proposed airborne Doppler lidar. Sections VI and VII present an analysis of LESs generated by Boeing 747 (B747) and Boeing 757 (B757) wake vortices and of detection results when these vortices are applied to the Doppler lidar simulation.

IV. LES of Wake Vortices

Computations of three-dimensional wake vortex evolutions were performed by CERFACS using two LES methods:

1) NTMIX[9]: a high-order Navier–Stokes solver that is used to model vortex behavior in Homogeneous Isotropic Turbulence (HIT). This method is used to model vortex behavior when convection is not a factor.

2) Meso-NH[10]: an atmospheric simulation system that is used to model vortex behavior in an atmospheric boundary layer (ABL).

This method is used to model vortex behavior in the presence of convective turbulence that occurs close to the ground.

A. NTMIX Solver

The present NTMIX code solves three-dimensional unsteady compressible Navier–Stokes equations. A highly accurate finite difference method over a Cartesian grid is used to fully handle most of the different scales in the three-dimensional flow: spatial derivatives are computed with a sixth-order compact scheme (Padé scheme[11]) that has the property of being low-dispersive and nondissipative. Time advancement is achieved with a third-order Runge–Kutta method. The code uses the Navier–Stokes characteristic boundary conditions (NSCBC) method[12] and supports different types of boundary conditions, including nonreflecting open boundary conditions and adiabatic or isothermal solid walls.

The LES approach is based on the filtering of the complete compressible Navier–Stokes equations (due to the finite mesh size), which exhibit subgrid scale tensors and vectors describing the interaction between nonresolved (subgrid scales) and resolved motion. The influence of nonresolved scales on the resolved motion is taken into account by means of a subgrid scale model based on the introduction of a turbulent viscosity ν_t (Ref. 13).

The model chosen for ν_t is the filtered structure function model.[14,15] The velocity measure of the small scale turbulent structures is estimated through a second-order structure function $\tilde{F}_2$, based on high-pass filtered velocity fields $HP^{(3)}\boldsymbol{u}$. This process yields

$$\begin{aligned}\tilde{F}_2(\boldsymbol{x},\Delta,t) = \tfrac{1}{6}\Big[&\left\| HP^{(3)}\boldsymbol{u}_{i+1,j,k} - HP^{(3)}\boldsymbol{u}_{i,j,k}\right\|^2 \\ &+ \left\| HP^{(3)}\boldsymbol{u}_{i-1,j,k} - HP^{(3)}\boldsymbol{u}_{i,j,k}\right\|^2 \\ &+ \left\| HP^{(3)}\boldsymbol{u}_{i,j+1,k} - HP^{(3)}\boldsymbol{u}_{i,j,k}\right\|^2 \\ &+ \left\| HP^{(3)}\boldsymbol{u}_{i,j-1,k} - HP^{(3)}\boldsymbol{u}_{i,j,k}\right\|^2 \\ &+ \left\| HP^{(3)}\boldsymbol{u}_{i,j,k+1} - HP^{(3)}\boldsymbol{u}_{i,j,k}\right\|^2 \\ &+ \left\| HP^{(3)}\boldsymbol{u}_{i,j,k-1} - HP^{(3)}\boldsymbol{u}_{i,j,k}\right\|^2\Big] \end{aligned} \tag{1}$$

where the three-dimensional high-pass filter is defined by

$$\begin{aligned}HP^{(1)}\boldsymbol{u}(\boldsymbol{x},t) = {}&\boldsymbol{u}_{i+1,j,k} - 2\boldsymbol{u}_{i,j,k} + \boldsymbol{u}_{i-1,j,k} + \boldsymbol{u}_{i,j+1,k} \\ &- 2\boldsymbol{u}_{i,j,k} + \boldsymbol{u}_{i,j-1,k} + \boldsymbol{u}_{i,j,k+1} - 2\boldsymbol{u}_{i,j,k} + \boldsymbol{u}_{i,j,k-1}\end{aligned} \tag{2}$$

with $HP^{(3)}\boldsymbol{u} = HP^{(1)}[HP^{(1)}(HP^{(1)}u)]$. The meaning of the index i, j, k notation is straightforward for the structured finite difference numerical method we use. The eventual formulation reads

$$\nu_t(\boldsymbol{x},t) \approx 0.0014 C_K^{-\frac{3}{2}} \Delta \left[\tilde{F}_2^{(3)}(\boldsymbol{x},\Delta,t)\right]^{\frac{1}{2}} \tag{3}$$

where Δ stands for the mesh size and $C_K = 1.4$ is the Kolmogorov constant. The latter equality expresses the fact that the model is required to provide the same amount of dissipation as a homogeneous incompressible turbulence of the same energy at the cutoff.[14] Moreover, the model has been shown to behave well for isotropic turbulence and to provide realistic simulations of the transition to turbulence in unstable flows.

B. Meso-NH Atmospheric Simulation System

The Meso-NH Atmospheric Simulation System is a joint effort of the Centre National de Recherches Météorologiques (Météo-France) and the Laboratoire d'Aérologie (Centre National de la Recherche Scientifique).

This model is based on the Lipps and Hemler[16] ($\partial\rho/\partial t = 0$) modified anelastic system[17] in order to avoid a very strong constraint on the computational time step. In this approach, the acoustic waves are eliminated from the continuous set of equations by the use of a constant density profile instead of the actual fluid density in the continuity equation and in the momentum equation. This is not done for the buoyancy term, which is the leading term of the approximation. The fluid, therefore, becomes formally incompressible, and the pressure is deduced from the solution of an elliptic equation.

The data used for initialization are taken from the 1990 Idaho Falls (IDF) field experiment.[18] The ABL was high, and its approximate altitude can be computed using

$$h^2 = h_0^2 + 2(Q/A)(t - t_0) \tag{4}$$

where h_0 is the known altitude at t_0, Q the ground heat flux ($\cong$0.5 W m^{-2}) and A the temperature gradient in the stable layer above the ABL ($\cong$0.02 K m^{-1}). Then h is assumed equal to 950 m. The experimental data are extrapolated to this altitude. We assume also that the ground is adiabatic and that the heat flux is constant (equal to Q). For the computation of the turbulent background field, the grid steps are $\Delta x = \Delta y = 5$ m. A vertical stretching is imposed: $\Delta z = 1$ m up to 90 m and then stretched up to 2000 m. The initial grid mesh is $40 \times 40 \times 140$. The simulation with Meso-NH gives an ABL of 1000 m with atmospheric vortices of up to 1 km in diameter. In this case, the vertical velocities in the mixing layer are about 2 m s^{-1}.

We use the "dry" potential temperature as a thermodynamic variable. We only consider dry air here because Idaho Falls is a very dry area. Before introducing the trailing vortices, the ABL results are spawned onto a $180 \times 36 \times 140$ Cartesian grid in order to increase the accuracy of the computation.

C. Wake Vortex Pair Initialization

To define the initial conditions for the simulations, we have used analytic expressions for the vortices. The Lamb–Oseen vortex was chosen. It is an unsteady solution of the Navier–Stokes equations for the evolution of an initial line vortex characterized by a circulation Γ (see Lamb,[19] p. 592). If the cylindrical coordinates (r, θ, z) are considered, the induced velocity $\boldsymbol{u}$ is only azimuthal, and its spatial distribution depends only on the radius

$$u_\theta(r) = \alpha V_0 (r_c/r)\left\{1 - \exp\left[-\beta(r/r_c)^2\right]\right\} \tag{5}$$

with $\alpha = 1.40$ and $\beta = 1.2544$ (Ref. 20). The circulation of each vortex is then given as

$$\Gamma = 2\pi\alpha V_0 r_c \tag{6}$$

It must be noted that no axial velocity is initialized.

In NTMIX, the pressure P is also initialized by the integration of

$$\frac{\mathrm{d}P}{\mathrm{d}r} = \rho\frac{u_\theta^2}{r} \tag{7}$$

The vortex pair consists of two vortices parallel to the z-axis with a spacing b_0 in the x-direction. The flowfield of the pair is obtained by the linear superimposition of the velocity and pressure fields. This superimposition is valid until the distance b_0 is equal to several core radii.

V. Simulation of Airborne Doppler Lidar

The lidar simulation takes the three-dimensional flowfield data generated by the LES as its primary input (see Fig. 2). The other inputs are the operational parameters of the lidar and a geometric definition of the scanning pattern.

For this study, we have simulated a 2-μm coherent lidar system with the parameters given in Table 1. These performance parameters

Table 1 Parameters defining the simulated lidar system

Parameter	Value
Pulse energy	3 mJ
Pulse repetition frequency	500 Hz
Pulse duration (full-width at half maximum)	413 ns
Local oscillator frequency offset	30 MHz
Aperture radius	50 mm
System efficiency (far field)	0.1
Real sampling frequency	128 MHz
Laser wavelength	2.02184 μm
Focal length	2000 m
Range gate length	75 m

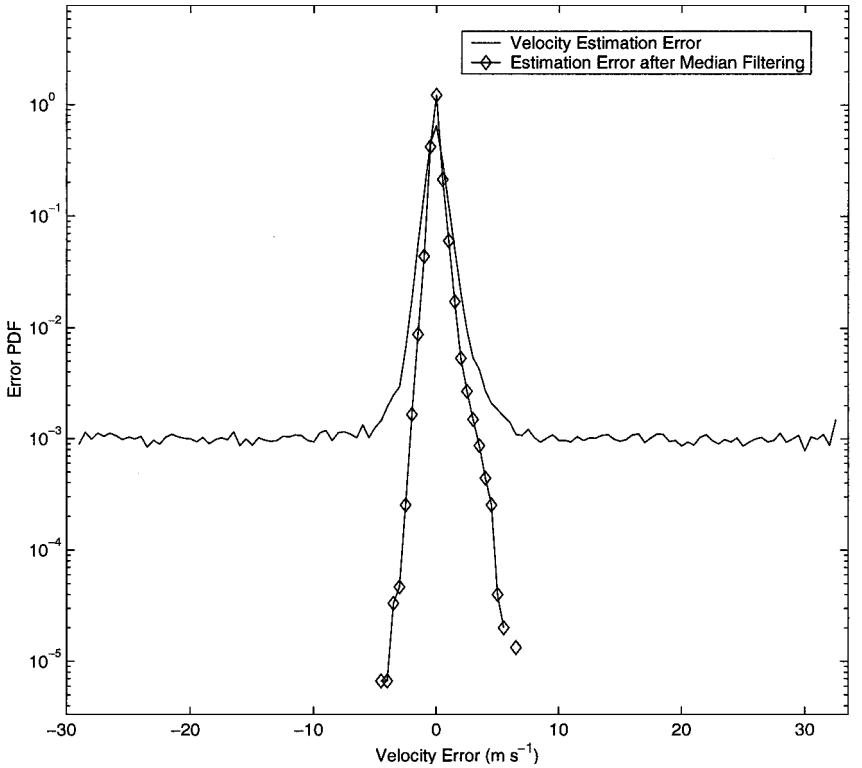

Fig. 3 Probability distribution function of the velocity estimation error and the same data after second median filtering of the constructed radial velocity images.

are similar to those already achieved in airborne systems. Real sampling of the lidar signal is simulated. The frequency offset between the pulsed laser and the local oscillator laser of 30 MHz allows for differentiation between negative and positive Doppler shifts without complex sampling.

A. Lidar Signal Simulation

A time domain simulation, introduced by Salamitou et al.[21] and Frehlich,[22] is used to simulate the backscattered lidar signal at each scan position. Inputs to the time domain simulation are the set of wind vectors, calculated at 1-m intervals along each line of sight by three-dimensional interpolation of the simulated flowfields, and the signal-to-noise ratio along each line of sight, which is calculated from the lidar parameters and the atmospheric parameters with the equation given by Targ et al.[23] For this study, the atmospheric parameters are taken from a midlatitude summer atmospheric model.

B. Scanning the Field of View

We have simulated a two-dimensional raster-type scanning of the airspace in front of the aircraft with an angular scanning resolution of 0.15 deg in the horizontal and the vertical. This resolution results in a transverse spatial resolution of approximately 3 m at a distance of 1000 m from the scanner and of approximately 6 m at a range of 2000 m from the scanner. As an exact raster scanning pattern may be difficult to realize mechanically, we have also investigated a sinusoidal scanning pattern and have found that, with appropriate modifications to the image processing implementation, similar system performance can be achieved.

Because of vortex sinking and lateral movement, the wake vortices can move out of the field of view as they evolve. To compensate for this effect, the vortices are moved to the approximate center of the field of view before scanning is implemented.

C. Signal Processing

The lidar simulation generates a sampled signal, which represents the output of the photodetector after sampling. The simulated lidar signal is sectioned into consecutive range gates of 64 samples, corresponding to range gate of length 75 m. The Doppler shift within each range gate is estimated by taking the frequency of the peak of the periodogram.[24] A fast Fourier transform is used to calculate the periodogram, and zero-padding is used to increase the spectral frequency resolution to 0.5 MHz. For a 2-μm lidar, these parameters correspond to a velocity resolution of 0.5 m s^{-1}.

To assess the accuracy of the peak of the periodogram as a Doppler shift estimator, the true Doppler shift at each range gate must be calculated. This shift can be calculated from the mean pulse-weighted velocity over each range gate[22] by convolving the true line-of-sight velocities with the normalized pulse shape and then averaging over the range gate length. The estimation accuracy is described by the probability density function (PDF) of the estimation error. For an unbiased estimator, this error PDF is characterized by a local distribution of good estimates centered at 0 m s^{-1} and a uniform distribution of spurious estimates spread throughout the velocity search space.[25] Spurious estimates result from range gates in which destructive interference (i.e., speckle) in the backscattered signal causes the signal level to fade into the noise floor, and a spurious peak is chosen as the shift estimate.

A typical PDF of the velocity estimation error achieved during our simulation is shown in Fig. 3. Figure 3 illustrates that the peak of the frequency spectrum is an unbiased estimator of the Doppler shift and that approximately 6% of all of the estimates are spurious.

D. Image Processing

At the end of each complete scan, radial velocity estimates from range gates that are at equal distances from the scanner are combined to form radial velocity images. Since a complete scan of the field of view takes a finite duration, the forward movement of the aircraft is considered when constructing the range gates that form these radial images.

The radial velocity images are noisy because approximately 6% of the radial velocity estimates that make up these images are spurious. A number of image-processing algorithms have been investigated

with the aim of reducing image noise, and two-dimensional median filtering has been found to be effective at reducing the number of spurious estimates without distorting the underlying radial velocity image. Figure 3 shows the error PDF before and after image processing. Note that, after median filtering, the spurious estimates were completely removed.

Visual identification of vortex signatures is usually possible from the image-processed radial velocity images. Alternatively, pattern recognition techniques can be applied in order to detect wake vortex signatures and then automatically issue a warning to the pilot.

In this paper, we present radial velocity images constructed at a range of 2000 m ahead of the airborne Doppler lidar. Vortex detection at this range would give the pilot reasonable time in which to take evasive action. However, radial velocity images can be constructed at any range up to 2000 m from the Doppler lidar system. In fact, the estimated radial velocity images become more accurate closer to the Doppler lidar, as the signal-to-noise ratio and the transverse spatial resolution both increase. Results from ranges between 500 and 2000 m ahead of the aircraft can be combined to form a plan-position indicator (PPI) that presents an intuitive plan view of the airspace in front of the aircraft. In the event that a wake vortex enters the intended airspace of the follower, the PPI view could be used by the pilot to avoid the otherwise invisible vortex hazard.

VI. B747 Wake Vortices in a Homogeneous Isotropic Turbulence

A. LES Details

The B747 simulation uses the NTMIX solver on a $64 \times 64 \times 64$ Cartesian grid, with each dimension of the computational domain having periodic boundaries with sides of length $28 \times r_c$. For this, the Reynolds number is set to 10×10^6, and the magnitude of the fluctuation velocities set to 10% of the maximum tangential velocity.

The kinetic energy spectrum of the flow prior to injection of the vortices is plotted in Fig. 4 and shows that the kinetic energy spectrum has a slope of $k^{-5/3}$. This result is very close to what is expected for the inertial range and validates the numerical scheme and the LES model for this type of application.

A Lamb–Oseen vortex pair with parameters roughly corresponding to a rolled up B747 wake ($\Gamma = 600$ m^2 s^{-1}, $r_c = 5$ m, and $b_0 = 48$ m) is superimposed on the ambient turbulence field. Figure 5 shows the magnitude of λ_2, where λ_2 is the second eigenvalue of the symmetric tensor $S^2 + \Omega^2$ and S and Ω are, respectively, the symmetric and antisymmetric parts of the velocity gradient tensor $\nabla \boldsymbol{u}$. This parameter, defined by Jeong and Hussain,[26] was demonstrated to be very efficient at capturing vortices in a turbulent background. One can see ring structures rolling around the vortices. These structures, which do not exist at the beginning of the simulation, are created by the action of the vortices on the ambient turbulence.

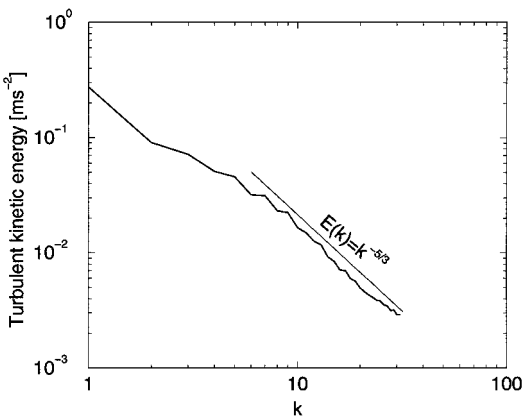

Fig. 4 Turbulence spectra of the homogeneous isotropic turbulence field just prior to injecting the vortices.

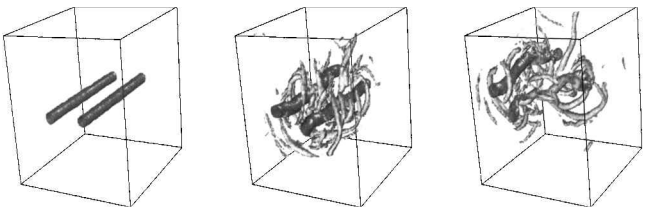

Fig. 5 Iso-surfaces of λ_2 at several time instants ($t^* = 0$, 60, and 120) for a vortex pair placed in moderate homogeneous isotropic turbulence. The LESs were performed with a sixth-order compact scheme.

For this test case, we observed that the wake vortex decay is quite typical: the circulation is reduced by 50% after 50 s.

B. Flowfield Analysis

Figure 6 presents horizontal cross sections through the cores of B747 wake vortices evolving in HIT showing the vertical wind component (left) and the axial wind component (right).

The decay of the vortex pair with time is illustrated in the set of vertical wind component cross sections. Note that one vortex decays more quickly than the other. In the cross sections at age 43.8 and 54.5 s, one can also see the initiation of long wavelength instability. The wavelength of this instability is fixed by the domain size.

This vortex pair was initialized without axial velocity at age 9 s. At age 12 s, weak axial velocity components become evident. By age 22.6 s, strong axial velocities have been induced in both vortices, and these components have strengthened further by age 33.2 s. These velocity components are induced in both axial directions. We attribute this induction to the process described by Batchelor.[8]

These lengths of the induced axial velocities sections are important from a detection point of view. Correlation between the spatial volume of a lidar pulse and the induced axial velocity sections is necessary in order to reliably detect the axial velocities. In this case, one can observe continuous sections of axial velocity of between 30 and 60 m in each direction. These sections are of the same order as the spatial pulse length of the proposed detection system, which was chosen to be 75 m.

C. Applying the Flowfields to the Lidar Simulation

The results shown in Fig. 7 were generated by applying the LES flowfields to the airborne lidar simulator. At each age shown, the true radial velocity, calculated as the mean of the pulse-weighted velocity over each range gate, is shown on the left, while the radial velocity image generated by the lidar simulation is shown on the right. The radial velocities detected by the lidar are in good agreement with the calculated true radial velocities.

The main result is that the vortices are detectable from their induced axial components at ages 22–54 s.

D. Comment

The scenario simulated here does not correspond to actual flight conditions, as a following aircraft will usually maintain a fixed separation from the leading aircraft and so could only encounter wake vortices of fixed age. However, simulating a vortex pair evolving 2000 m ahead of the Doppler lidar system allows us to demonstrate that vortices of varying ages are detectable from their axial signatures, using a forward looking Doppler lidar system. In this case, the B747 vortex pair is detectable between ages 22 and 54 s at a range of 2000 m. This range corresponds to the scenario where the B747 generating the vortices is between 3650 and 6050 m ahead of the aircraft carrying the Doppler lidar system (assuming an approach speed for both aircraft of 75 m s^{-1}). Such separations are considerably less than current IFR recommendations of 4 n mile (7408 m) for a heavy aircraft behind a B747 and of 5 n mile (9260 m) for a large aircraft behind a B747.

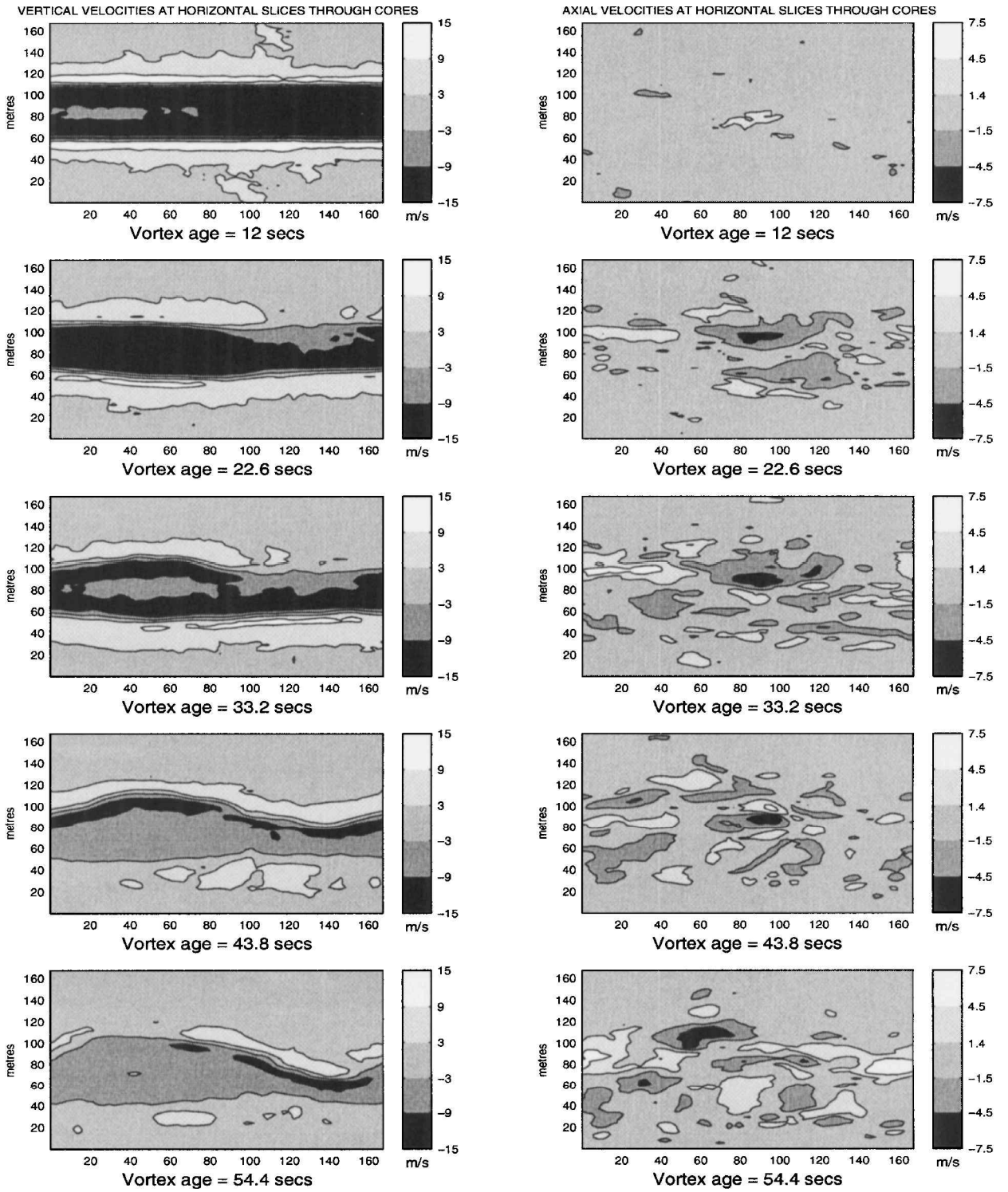

Fig. 6 Horizontal slices through cores of B747 wake vortices evolving in homogeneous isotropic turbulence showing vertical wind components (left) and axial wind components (right) as contour plots. The axes of the vortices are initially horizontal. The x and y axes are in meters. The vortices have been laterally shifted to the approximate center of the simulation box in order to facilitate graphical comparison.

VII. B757 Wake Vortices in a Convective ABL

A. LES Details

In this section, we present results based on the run 30 of the Boeing 757 at Idaho Falls. A more detailed study of this run performed with Meso-NH has been presented by Corjon et al.[27] The parameters of the vortex pair are $\Gamma = 360\ \mathrm{m^2\,s^{-1}}$, $r_c = 3$ m, and $b_0 = 30$ m. The three-dimensional iso-surface of vorticity magnitude ($\Omega = 20\ \mathrm{s^{-1}}$) is presented in Fig. 8 for different ages. At $t = 0$, the highest level of vorticity is concentrated in the vortex core. As they evolve, the vortices create azimuthal structures moving around the wake vortices. Vortex stretching is responsible for the creation of these structures. The entropy between the two vortices increases with the formation of these eddies, and there is also a creation of strong axial velocities.

The average position of each vortex is plotted vs time in Fig. 9. The extremas of positions of the centers (error bars) illustrate that the vortex bending, due to Crow instability[28] and to convective, effects increases with time. Wake vortex trajectories from field measurements are also shown, comparing well with our simulations.

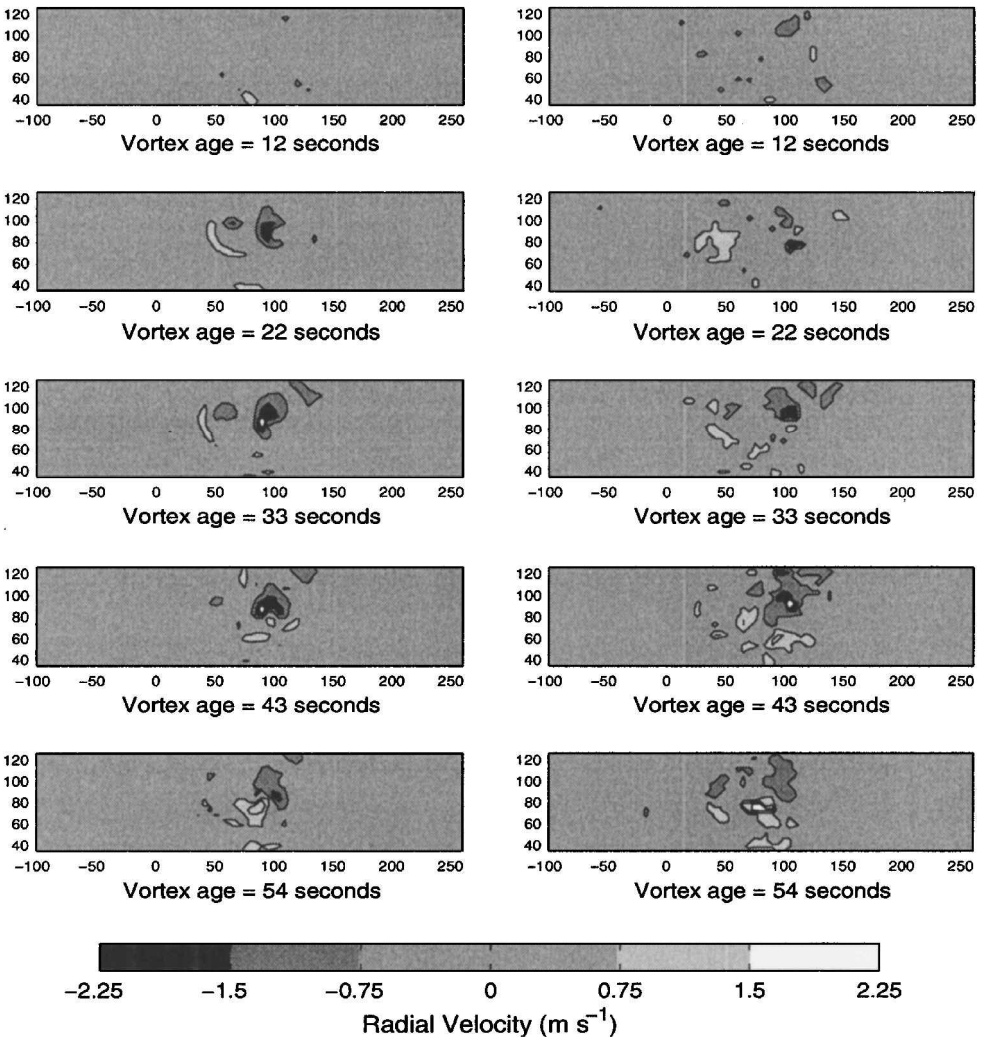

Fig. 7 Velocity images generated by simulating the forward looking Doppler lidar system encountering wake vortices from a B747 that are evolving in homogenous isotropic turbulence. These velocity images have been formed 2000 m ahead of the following aircraft. The contour plots on the left are generated from the mean pulse-weighted radial velocity over the range gate, whereas the plots on the right are the radial velocity images estimated by the lidar system.

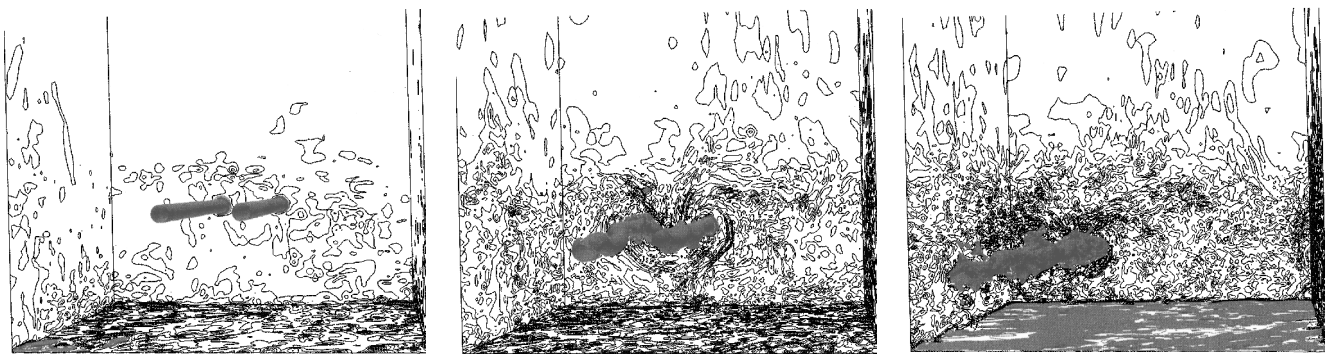

Fig. 8 Iso-surface of vorticity magnitude at times t = 0, 10, 20 s. The LESs of IDF run 30 case were performed with a meteorological solver.

B. Flowfield Analysis

Figure 10 presents horizontal cross sections through the cores of B757 wake vortices evolving in ABL turbulence showing vertical wind component (left) and axial wind component (right). From the vertical wind component set of cross sections, it is clear that this vortex decays more rapidly than the HIT case. At age 38 s, the initiation of Crow instability is evident, whereas at age 48 s, the vortices are significantly decayed.

In the right-hand set of cross sections shown in Fig. 10, the axial velocity is shown. This vortex pair was initialized without axial velocity at age 8 s. By age 18 s, axial velocities in each direction have developed in both vortices. These axial components strengthen until the vortex is aged 38 s and then decay as the vortices themselves decay. The length of the axial velocity sections in both direction is between 40 and 60 m for each vortex.

C. Lidar Detection of B757 Simulated Wake Vortices

The results shown in Fig. 11 were generated by applying the LES flowfields to the airborne lidar simulator. As before, the true radial velocity, calculated as the pulse-weighted velocity over each range

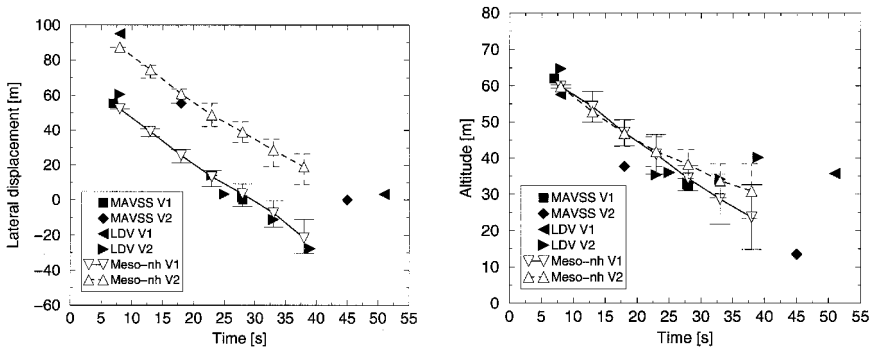

Fig. 9 Trajectory of the vortex pair, error bars indicate the vertical shifting of the centers. The LESs of IDF run 30 case were performed with a meteorological solver. Wakes have been measured by a laser Doppler velocimeter (LDV), an array of monostatic acoustic vortex sensing system (MAVSS), and a 60-m instrumented tower.

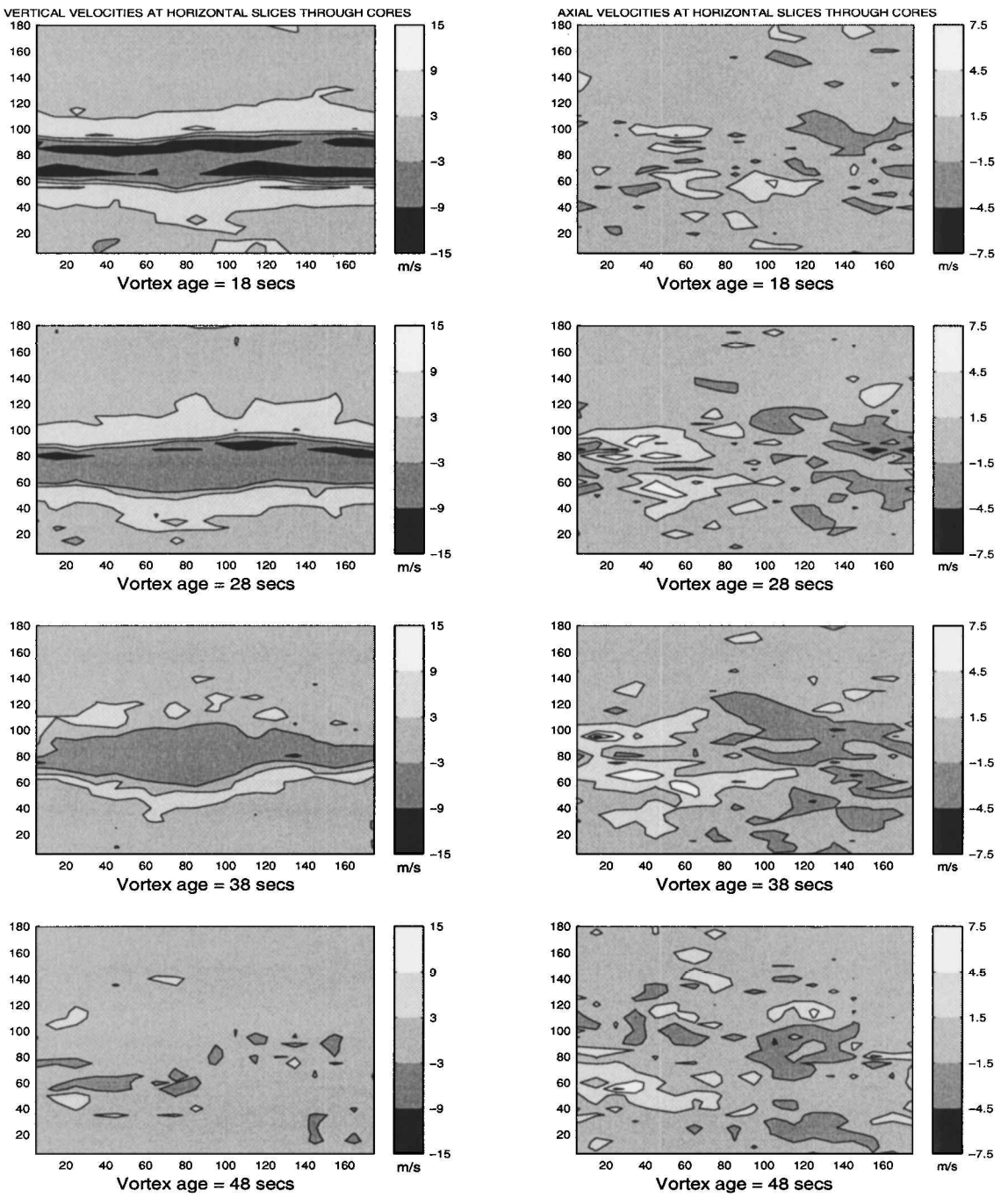

Fig. 10 Horizontal slices through cores of B757 wake vortices evolving in atmospheric convective turbulence showing vertical wind component (left) and axial wind component (right). The axes of the vortices are initially horizontal. The *x* and *y* axes are in meters. The vortices have been laterally shifted to the approximate center of the simulation box in order to facilitate graphical comparison.

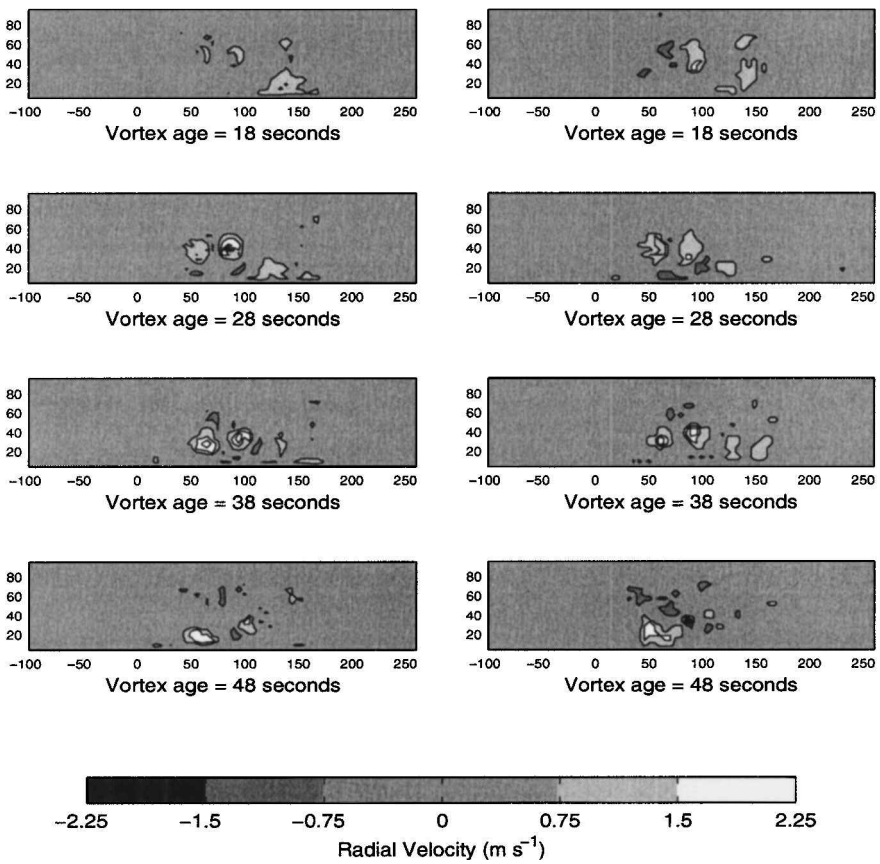

Fig. 11 Velocity images generated by simulating the forward-looking Doppler lidar system encountering wake vortices from a B757 that are evolving in a convective ABL. These velocity images have been formed 2000 m ahead of the following aircraft. The contour plots on the left are generated from the mean pulse-weighted radial velocity over the range gate, whereas the plots on the right are the radial velocity images estimated by the lidar system.

gate, is shown on the left, whereas radial velocity image generated by the lidar simulation is shown on the right. The radial velocities detected by the lidar are in good agreement with the calculated true radial velocities.

The main result is that the vortices are detectable from their induced axial components between ages 18 and 48 s.

D. Comment

In this case, the B757 vortices are detected by the lidar simulator between ages 18 and 48 s at a range of 2000 m. As before, there is a correlation with the analysis in Sec. VII.B based on Fig. 10 which shows the presence of significant axial velocity components at all ages. Vortices between ages 18 and 48 s detected 2000 m ahead would be generated by a B757 flying between 3350 and 5600 m ahead of the aircraft carrying the Doppler lidar system (assuming an approach speed for both aircraft of 75 m s^{-1}). Such separations are less than the recommended separation behind a B757.

VIII. Conclusions

Three-dimensional LES of wake vortices have shown that axial flows are induced in the cores as the vortices evolve. Analysis of the induced flows indicates that they are of sufficient size and magnitude to be detectable with a pulsed Doppler lidar.

The flowfields generated by the LES were then applied to a software simulation of an airborne 2-μm pulsed Doppler lidar. Results have shown that the proposed system could detect wake vortices generated by a leading aircraft at ranges up to 2 km ahead of the following aircraft.

We propose that an aircraft fitted such a system could follow with reduced separation without compromising safety. In the event that a wake vortex remains stable and in the flight path of the follower, the detection system would allow reasonable time in which to take evasive action.

Acknowledgments

This work was performed within the Multifunction Future Laser Atmospheric Measurement Equipment (MFLAME) project, which is supported by the European Communities in the frame of the fourth Framework Research Programme under Brite Euram Contract BE95-1541. The authors acknowledge the direct and indirect contribution of all of the partners in the MFLAME project to the work carried out for this paper.

References

[1]Reimer, H. M., and Vicroy, D. D., "A Preliminary Study of a Wake Vortex Encounter Hazard Boundary for a B737-100 Airplane," NASA TM 110223, April 1996.

[2]Perry, R. B., Hinton, D. A., and Steuver, R. A., "NASA Wake Vortex Research for Aircraft Spacing," AIAA Paper 97-0057, Jan. 1997.

[3]Hannon, S., and Thompson, J. A., "Aircraft Wake Vortex Detection and Measurement with Pulsed Solid-State Coherent Laser Radar," *Journal of Modern Optics*, Vol. 41, No. 11, 1994, pp. 2175–2196.

[4]Huffaker, R. M., and Hardesty, R. M., "Remote Sensing of Atmospheric Wind Velocities Using Solid-State and CO2 Coherent Laser Systems," *Proceedings of the IEEE*, Vol. 84, No. 2, 1996, pp. 181–204.

[5]Richmond, R., and Jewell, J., "U.S. Air Force Ballistic Wind Program," *9th Conference on Coherent Laser Radar*, FOA Repro, Linkoping, Sweden, 1997, pp. 304–307.

[6]Hannon, S. M., Bagley, H. R., and Bogue, R. K., "Airborne Doppler Lidar Turbulence Detection: ACLAIM Flight Test Results," *Laser Radar Technology and Applications IV*, SPIE Proceedings Vol. 3707, International Society for Optical Engineering, Bellingham, WA, 1999, pp. 234–241.

[7]Brown, C. E., "Aerodynamics of Wake Vortices," *AIAA Journal*, Vol. 11, No. 4, 1973, pp. 531–536.

[8]Batchelor, G., "Axial Flow in Trailing Line Vortices," *Journal of Fluid Mechanics*, Vol. 20, No. 4, 1964, pp. 645–658.

[9]Stoessel, A., "An Efficient Tool for the Study of 3D Turbulent Combustion Phenomena on MPP computers," *Proceedings of the High Performance Computing and Networks 95 Conference*, Springer-Verlag, 1995, pp. 306–311.

[10]Lafore, J. P., Stein, J., Asencio, N., Bougeault, P., Ducrocq, V., Duron, J., Fischer, C., Héreil, P., Mascart, P., Masson, V., Pinty, J. P., Redelsperger, J. L., Richard, E., and Vilà-Guerau de Arellano, J., "The Meso-NH Atmospheric Simulation System. Part I: Adiabatic Formulation and Control Simulations," *Annales Geophysicae*, Vol. 16, No. 1, 1998, pp. 90–109.

[11]Lele, S. K., "Compact Finite Difference Schemes with Spectral-Like Resolution," *Journal of Computational Physics*, Vol. 103, Nov. 1992, pp. 16–42.

[12]Poinsot, T., and Lele, S., "Boundary Conditions for Direct Simulations of Compressible Viscous Flows," *Journal of Computational Physics*, Vol. 101, July 1992, pp. 104–129.

[13]Ducros, F., Comte, P., and Lesieur, M., "Large-Eddy Simulation of Spatially Growing Boundary Layer over an Adiabatic Flat Plate," *International Journal of Heat and Fluid Flow*, Vol. 16, No. 5, 1995, pp. 341–348.

[14]Ducros, F., Comte, P., and Lesieur, M., "Large-Eddy Simulation of Transition to Turbulence in a Weakly Compressible Boundary Layer over a Flat Plate," *Journal of Fluid Mechanics*, Vol. 326, 1996, pp. 1–36.

[15]Lesieur, M., and Métais, O., "New Trends in Large-Eddy Simulations of Turbulence," *Annual Review of Fluid Mechanics*, Vol. 28, 1996, pp. 45–82.

[16]Lipps, F., and Hemler, R., "A Scale Analysis of Deep Moist Convection and Some Related Numerical Calculations," *Journal of Atmospheric Sciences*, Vol. 39, No. 10, 1982, pp. 2192–2210.

[17]Ogura, Y., and Phillips, N., "Scale Analysis of Deep and Shallow Convection in the Atmosphere," *Journal of Atmospheric Sciences*, Vol. 19, No. 2, 1962, pp. 173–179.

[18]Garodz, L. J., and Clawson, K. L., "Vortex Wake Characteristics of B757-200 and B767-200 Aircraft Using the Tower Fly-by Technique," ERL ARL-199 Vols. 1 and 2, National Oceanic and Atmospheric Administration, Idaho Falls, ID, Jan. 1993.

[19]Lamb, H., *Hydrodynamics*, 6th ed., Dover, New York, 1932, Chap. 11, p. 592.

[20]Corjon, A., Risso, F., Stoessel, A., and Poinsot, T., "3D Direct Numerical Simulations of Wake Vortices: Atmospheric Turbulence Effects and Rebound with Crosswind," *78th Fluid Dynamics Panel Symposium on the Characterization and Modification of Wakes from Lifting Vehicles in Fluids*, CP-584, AGARD, Trondheim, Norway, 1996, pp. 28-1–28-21.

[21]Salamitou, P., Dabas, A., and Flamant, P., "Simulation in the Time Domain for Heterodyne Coherent Laser Radar," *Applied Optics*, Vol. 34, No. 3, 1995, pp. 499–506.

[22]Frehlich, R., "Effect of Wind Turbulence on Coherent Doppler Lidar Performance," *Journal of Atmospheric and Oceanic Technology*, Vol. 14, No. 1, 1997, pp. 54–75.

[23]Targ, R., Kavaya, M., Huffaker, R., and Bowles, R., "Coherent Lidar Airborne Windshear Sensor: Performance Evaluation," *Applied Optics*, Vol. 30, No. 15, 1991, pp. 2013–2026.

[24]Oppenheim, A., and Schafer, R., *Discrete Time Signal Processing*, Prentice–Hall, Upper Saddle River, NJ, 1989.

[25]Rye, B., and Hardesty, R., "Detection Techniques for Validating Doppler Estimates in Heterodyne Lidar," *Applied Optics*, Vol. 36, No. 9, 1997, pp. 1940–1951.

[26]Jeong, J., and Hussain, F., "On the Identification of a Vortex," *Journal of Fluid Mechanics*, Vol. 285, 1995, pp. 69–94.

[27]Corjon, A., Darracq, D., Venzac, P., and Bougeault, P., "Three-Dimensional Large Eddy Simulation of Wake Vortices. Comparison with Field Measurements," AIAA Paper 98-0666, 1997.

[28]Crow, S., "Stability Theory for a Pair of Trailing Vortices," *AIAA Journal*, Vol. 8, No. 12, 1970, pp. 2172–2179.